

Phase and contrast moiré signatures in two-dimensional cone beam interferometry

D. Sarenac,^{1,2,*} G. Gorbet,³ Charles W. Clark,⁴ D. G. Cory,^{1,5} H. Ekinci,¹ M. E. Henderson,^{1,3} M. G. Huber,⁶ D. Hussey,⁶ C. Kapahi,^{1,3} P. A. Kienzle,⁶ Y. Kim,^{6,7} M. A. Long,⁸ J. D. Parker,⁹ T. Shinohara,⁹ F. Song,⁹ and D. A. Pushin^{1,3,†}

¹*Institute for Quantum Computing, University of Waterloo, Waterloo, ON, Canada, N2L3G1*

²*Department of Physics, University at Buffalo, State University of New York, Buffalo, New York 14260, USA*

³*Department of Physics, University of Waterloo, Waterloo, ON, Canada, N2L3G1*

⁴*Joint Quantum Institute, National Institute of Standards and Technology and University of Maryland, College Park, Maryland 20742, USA*

⁵*Department of Chemistry, University of Waterloo, Waterloo, ON, Canada, N2L3G1*

⁶*National Institute of Standards and Technology, Gaithersburg, Maryland 20899, USA*

⁷*University of Maryland, College Park, Maryland 20742, USA*

⁸*Materials Science and Technology Division, Los Alamos National Laboratory, Los Alamos, NM 87545, USA*

⁹*J-PARC Center, Japan Atomic Energy Agency (JAEA), 2-4 Shirakata, Tokai, Ibaraki 319-1195, Japan*

(Dated: November 7, 2023)

Neutron interferometry has played a distinctive role in fundamental science and characterization of materials. Moiré neutron interferometers are candidate next-generation instruments: they offer microscopy-like magnification of the signal, enabling direct camera recording of interference patterns across the full neutron wavelength spectrum. Here we demonstrate the extension of phase-grating moiré interferometry to two-dimensional geometries. Our fork-dislocation phase gratings reveal phase singularities in the moiré pattern, and we explore orthogonal moiré patterns with two-dimensional phase-gratings. Our measurements of phase topologies and gravitationally induced phase shifts are in good agreement with theory. These techniques can be implemented in existing neutron instruments to advance interferometric analyses of emerging materials and precision measurements of fundamental constants.

I. INTRODUCTION

Perfect-crystal neutron interferometry possesses a prestigious record of high impact fundamental science experiments such as the observation of gravitationally induced quantum interference [1], 4π symmetry of spinor rotation [2], neutron triply-entangled GHZ states and quantum discord [3, 4], matter-wave orbital angular momentum [5, 6], and the probing of dark energy and fifth forces [7, 8]. This is in-part due to the unique properties of the neutron such as its electrical neutrality, relatively large mass, and angstrom sized wavelengths [9–11]. Such properties also make the neutron a convenient and indispensable probe of modern materials as they are capable of characterizing bulk properties and nanometer-sized spin textures [12–15].

A recent focus in neutron interferometry has been in grating-based setups that circumvent the stringent environmental isolating requirements associated with perfect-crystal neutron interferometry [16, 17] and are capable of working in the full field of the neutron beam [18–24]. The backbone of these setups is the near-field phenomena of self-imaging known as the “Talbot effect” [25]. Further developments introduced phase-grating moiré interferometers (PGMIs) that are composed of exclusively phase-gratings and manifest interference patterns that

are directly detectable via typical neutron camera [26–31].

Here we take the next step in the development of the neutron PGMI toolbox by expanding to two-dimensional (2D) moiré interference. We explore the role of phase singularities that materials possessing helical structures are expected to induce in the moiré pattern and we describe the additional metrics for quantification. Furthermore, we also demonstrate 2D moiré interference with orthogonal directionality. The addition of an interference pattern serving as in-situ reference enables novel approaches for high precision measurements of fundamental forces such as the Newtonian constant of gravitation.

II. METHODS

We fabricated four types of phase-gratings: 2D phase-gratings, and fork-dislocation phase-gratings with topological charge of $q = 0, 4, 7$. Note that the $q = 0$ is a typical 1D phase-grating. The detailed nanofabrication procedure and scanning electron microscopy (SEM) images of all four cases can be found in Appendix A. All phase-gratings were fabricated out of silicon and had a target period of $3 \mu\text{m}$ and height of $8.53 \mu\text{m}$. The height of $8.53 \mu\text{m}$ was chosen so that the grating imparts an optimal $\pi/2$ phase shift for $\lambda = 9 \text{ \AA}$ neutrons.

The experiments with fork-dislocation phase-gratings were performed at the ASTERIX facility at the Los Alamos Neutron Science Center (LANSCE) [34]. The wavelength distribution is shown in Appendix B. The

* dsarenac@uwaterloo.ca

† dmitry.pushin@uwaterloo.ca

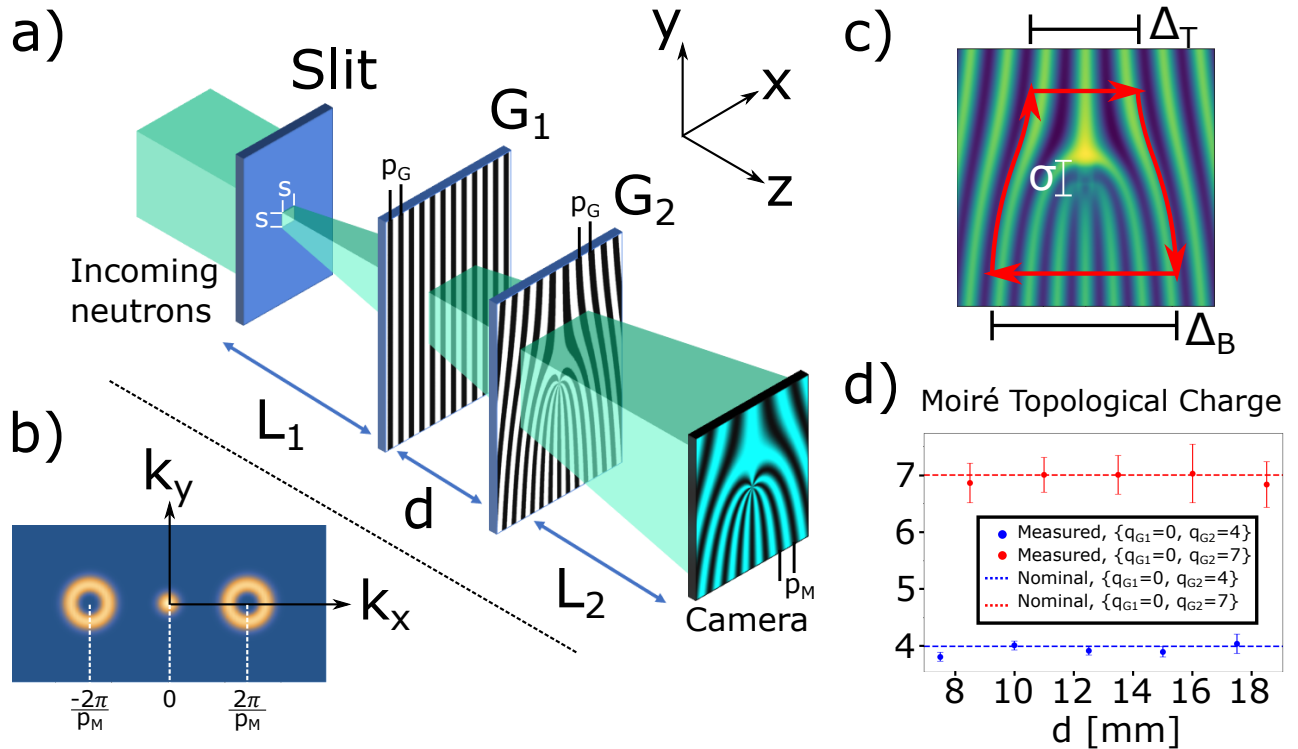


FIG. 1. a) The two-PGMI setup with fork-dislocation phase-gratings. In our experiments we employed and characterized $\{q_{G_1} = 0, q_{G_2} = 4\}$ and $\{q_{G_1} = 0, q_{G_2} = 7\}$ configurations. The moiré pattern at the camera manifests a phase-singularity with a topological charge of $q_M = \Delta q_G$ and with moiré period of $p_M = L p_G / d$, where L is the distance from the slit to camera, p_G is the period of the phase-gratings, and d is the distance between the two phase-gratings. b) The Fourier transform of the intensity pattern possesses doughnut-shaped diffraction orders indicative of helical phase structures [32]. c) Simulated intensity profile where the size of the smear (σ) centered on the phase-singularity is determined by the size of the slit (s). A convenient method of determining the topology in the measured intensity profile is given by $q_M = N_B - N_T$ where N_B (N_T) is the number of periods in a segment Δ_B (Δ_T) below (above) the origin where the connecting vertical lines (red arrows) between the two segments follow a trajectory of constant intensity [33]. d) The fitted topological charge of the observed moiré interference in our experiments for the $\{q_{G_1} = 0, q_{G_2} = 4\}$ and $\{q_{G_1} = 0, q_{G_2} = 7\}$ configurations. The uncertainties shown are statistical.

slit was $500 \mu\text{m}$ by $500 \mu\text{m}$ in size and the distance from the slit to the first phase-grating (camera) was 2.13 m (4.25 m). The camera pixel size was $50 \mu\text{m}$ by $50 \mu\text{m}$. The data acquisition time was $\approx 20 \text{ min}$ at each grating separation distance. A detector normalization image was obtained by summing phase stepping measurements.

The experiments with the 2D phase-gratings were performed at the the RADEN facility at the Japan Proton Accelerator Research Complex (J-PARC) [35]. The wavelength distribution is shown in Appendix B. The 2D slit was composed of a sequence of two perpendicular 1D slits each made by bringing two cadmium pieces together with the target gap of $500 \mu\text{m}$. Two experimental setups were used, one for polychromatic measurements and the other with a neutron camera with lower dark counts (≈ 0) for time-of-flight resolved measurements. For the first configuration the distance from the slit to the first phase-grating (camera) was 4.16 m (8.30 m), the camera pixel size was $100 \mu\text{m}$ by $100 \mu\text{m}$, and the image acquisition time was 4 h at each grating separation distance. For the second configuration the distance from the slit to the first phase-grating (camera) was 4.23 m (8.53 m),

the camera pixel size was $31 \mu\text{m}$ by $31 \mu\text{m}$, and the data acquisition time was 5 h . For each setup configuration a detector normalization image was obtained from a measurement at a setup configuration that results in zero contrast. Furthermore, due to the presence of significant salt and pepper noise a median filter of 5×5 pixels was applied to the final images.

III. RESULTS AND DISCUSSION

A. Fork-dislocation phase-gratings

Here we explore the effect of helical structures that manifest phase singularities in the moiré pattern by introducing a topological charge onto the phase-gratings themselves. A fork-dislocation phase-grating with period p_G , height D , and topological charge q_G has the profile:

$$\Phi = \frac{N b_c \lambda D}{2} \text{sgn} [\cos(k_G x + q_G \phi)] \quad (1)$$

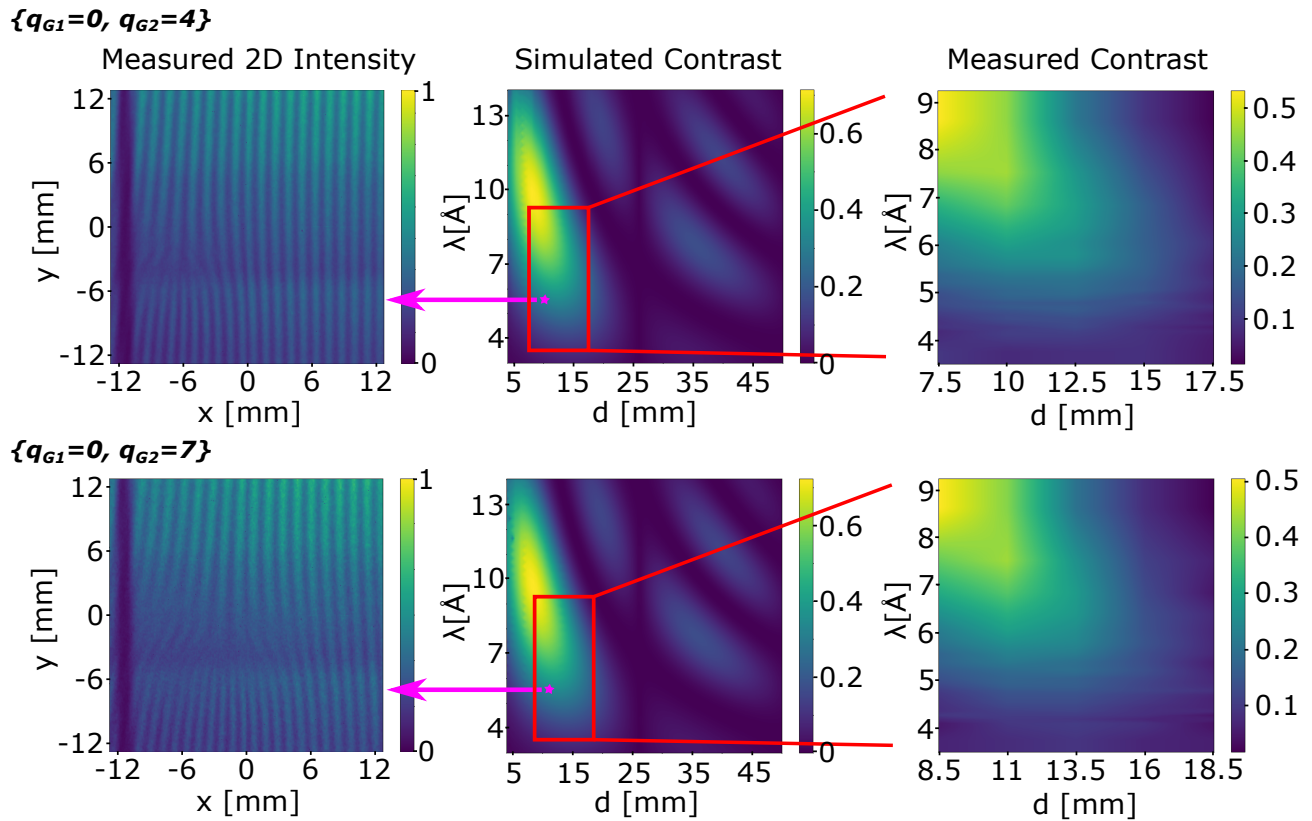


FIG. 2. The intensity and contrast behaviour of the two-PGMI setup with fork-dislocation phase-gratings. (First column) The observed 2D moiré intensity profile at the camera. (Second column) The simulated contrast as a function of wavelength and phase-grating separation distance. (Third column) The measured contrast for the accessible setup parameters. Top (bottom) row shows the setup for the $\{q_{G_1} = 0, q_{G_2} = 4\}$ ($\{q_{G_1} = 0, q_{G_2} = 7\}$) configuration. The 2D moiré pattern at the camera manifests a phase-singularity with topology $q_M = \Delta q_G$ as described in Fig. 1. The middle column depicts the contrast behaviour for a larger range of parameters, and indicates the parameters for the other two columns. The wavelength range for the the 2D moiré intensity profiles shown in the first column is $\lambda = 5 \text{ \AA} - 6 \text{ \AA}$ and the phase-grating separation is $d = 10 \text{ mm}$ (11 mm) for the $\{q_{G_1} = 0, q_{G_2} = 4\}$ ($\{q_{G_1} = 0, q_{G_2} = 7\}$) configuration.

where $k_G = 2\pi/p_G$ is the grating wave vector, $x(\phi)$ is the Cartesian (azimuthal) coordinate, N_{b_c} is the scattering length density of the grating material, and λ is the neutron wavelength. Using the recently introduced k-space model [36] we can simulate the intensity and contrast behaviour using the phase-grating profile of Eq. 1.

An experimental demonstration was performed with the two-PGMI configurations of $\{q_{G_1} = 0, q_{G_2} = 4\}$ and $\{q_{G_1} = 0, q_{G_2} = 7\}$. The first configuration is depicted on Fig. 1a. The moiré pattern at the camera possesses a topological charge of $q_M = \Delta q_G$ with moiré period of $p_M = Lp_G/d$, where L is the distance from the slit to camera, p_G is the period of the phase-gratings, and d is the distance between the two phase-gratings. The Fourier transform of the intensity profile is shown in Fig. 1b where the doughnut profiles are indicative of helical structures with phase singularities [32].

Whereas contrast is the figure of merit for a 1D two-PGMI, an additional metric is needed for identifying and characterizing phase singularities. In this particular setup the topology in the moiré pattern can be deter-

mined by $q_M = N_B - N_T$ where $N_B(N_T)$ is the number of periods in a segment $\Delta_B(\Delta_T)$ below (above) the origin where the connecting vertical lines between the two segments follow a trajectory of constant intensity [33], see Fig. 1c. Using this method we can calculate the measured moiré topology using a fit procedure for the two experimental configurations as shown in Fig. 1d. This method becomes increasingly useful as the smear centered on the phase-singularity increases with slit size.

Examples of the measured moiré pattern at the camera are shown in the first column of Fig. 2 for both $\{q_{G_1} = 0, q_{G_2} = 4\}$ and $\{q_{G_1} = 0, q_{G_2} = 7\}$. Note that the vertical stripe on the left is an upstream optical effect due to the guide geometry, and unrelated to the moiré interference. The simulated (measured) contrast as a function of phase-grating separation and wavelength is shown in the second (third) column of Fig. 2. The experimentally accessible parameters were not centered around the optimal contrast parameters as the phase-gratings were initially designed for a $\lambda = 9 \text{ \AA}$ neutrons. Good agreement is found between the predicted and measured con-

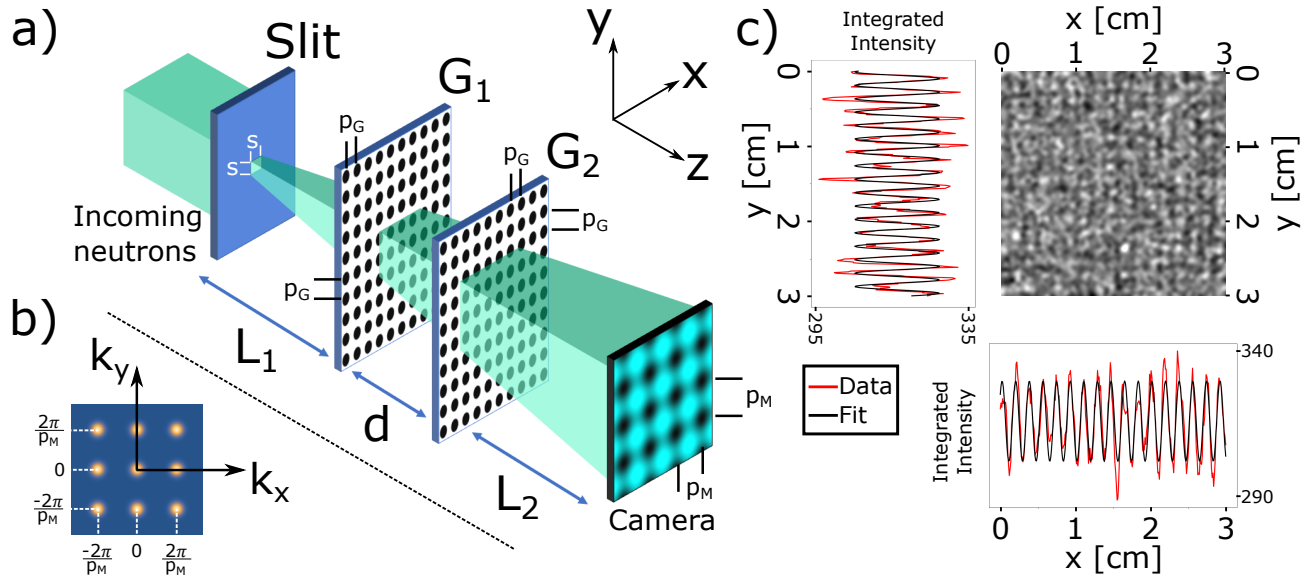


FIG. 3. a) The two-PGMI setup with two 2D phase-gratings. The moiré pattern at the camera manifests a 2D moiré pattern that possesses an x and y periodicity of $p_M = Lp_G/d$, where L is the distance from the slit to camera, p_G is the period of the phase-gratings, and d is the distance between the two phase-gratings. b) The Fourier transform of the intensity pattern shows 2D diffraction orders. c) The observed intensity profile at the camera can be integrated along x or y to independently analyze the contrast along the two orthogonal directions, thereby providing an in-situ reference signal when considering 1D forces and structures.

trast.

B. 2D phase-gratings

Here we aim to explore the 2D moiré pattern that possesses a periodicity along two orthogonal directions. There are many variations possible for 2D phase-grating profiles. For our experiments we chose a profile of:

$$\Phi = \frac{Nb_c\lambda D}{2} \text{sgn}[\cos(k_G x) + \cos(k_G y) - 1] \quad (2)$$

which is essentially a 2D array of circular holes as shown in the SEM images of Appendix A. The setup schematic is depicted on Fig. 3a. The 2D moiré pattern at the camera possesses a sinusoidal pattern in both the x and y directions. Therefore, its Fourier transform shows 2D diffraction orders as depicted in Fig. 3b. The 2D moiré pattern can be integrated along either Cartesian direction as shown in Fig. 3c where we consider the y -axis to be along Earth's gravity and the x -axis along the perpendicular direction. The shown profile is obtained by considering the phase-grating separation of $d = 12.5 \text{ mm}$ and $\lambda = 5 \text{ \AA} - 6 \text{ \AA}$ wavelength distribution, and the observed intensity profile at the camera has been rotated by $\theta = 13.3^\circ$ (corresponding to the maximum contrast location in a contrast vs θ plot).

The measured contrast as a function of phase-grating separation (d) for a polychromatic wavelength distribution is shown on Fig. 4a, and Fig. 4b shows wavelength-dependent contrast for a particular d . See Appendix B

for the wavelength distribution profile. Using the k -space model of Ref. [36] it can be confirmed that even when accounting for gravity the difference between the contrasts along the two directions should have been negligible for the given experimental parameters, and that the observed difference is most likely due to the difference in slit sizes. The 2D slit was composed of a sequence of two perpendicular 1D slits each made by bringing two cadmium pieces together with the target gap of $500 \mu\text{m}$. Performing a least squares fit to the two slit sizes we find good agreement with $643 \mu\text{m} \pm 49 \mu\text{m}$ for slit along x and $790 \mu\text{m} \pm 50 \mu\text{m}$ for slit along y . These values are well within the expected experimental uncertainties.

Fig. 4c shows the wavelength-dependent phase shift that can be used to quantify the effect of gravity. In a two-PGMI the main contribution to the gravitationally induced phase shifts is the neutron fall (Δ_y) between the second phase-grating and the neutron camera:

$$\phi_g = \frac{2\pi\Delta_y}{p_M} \cos\theta + C_0 = \frac{\pi g}{p_M} \left(\frac{L_2 m \lambda}{h} \right)^2 \cos\theta + C_0 \quad (3)$$

where θ is the angle between the moiré vector and the gravitational force vector, g is the acceleration due to Earth's gravity, m is the mass of the neutron, h is the Planck's constant, and C_0 is an arbitrary offset. We find good agreement between the expected and observed wavelength-dependent phase shifts.

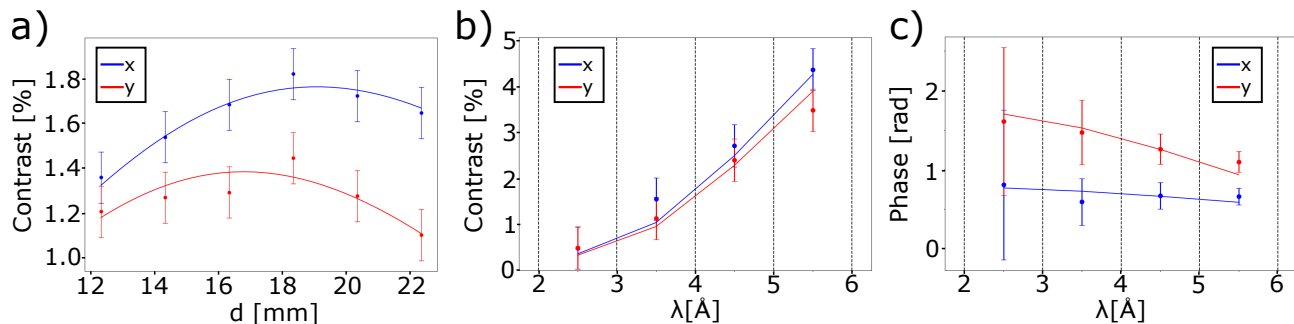


FIG. 4. a) The measured contrast of the two-PGMI setup with two 2D phase-gratings as a function of grating separation distance d and considering the full polychromatic wavelength distribution (see Appendix B). The simulation curves are obtained with the k-space model [36] for the given experimental parameters and with a least squares fit for the two slit sizes. The best fit is determined for $643 \mu\text{m} \pm 49 \mu\text{m}$ for the slit along x and $790 \mu\text{m} \pm 50 \mu\text{m}$ for the slit along y, which is well within the expected experimental error. b) The wavelength-dependent contrast along the x and y direction for $d = 12.5 \text{ mm}$. c) The wavelength-dependent phase shift along the x and y direction for $d = 12.5 \text{ mm}$. The wavelength distribution around each wavelength interval is shown in Appendix B. We find good agreement with the expected values when taking into account the gravitational fall from the second phase-grating to the camera and the relative rotation of $\theta = 13.3^\circ$ between the moiré vector and the Earth’s gravitational vector. The uncertainties shown are statistical.

IV. CONCLUSION

We have expanded neutron phase-grating moiré interferometry to 2D and enabled the use of new degrees of freedom for material characterization studies and high precision measurements of fundamental constants. We examined the manifestation and characterization of phase singularities in the moiré pattern by incorporating fork-dislocation phase-gratings. Future studies will look at the interference between multiple phase singularities and the effects that would be introduced by samples with phase singularities such as skyrmions [37, 38]. We also characterized two-PGMI setups that simultaneously manifest moiré interference along two orthogonal directions. The orthogonal interference pattern enables the presence of an in-situ reference signal that can greatly reduce systematic errors. Furthermore, future studies will also examine the use of 2D phase-linear gratings with three-PGMI where it is possible to substantially increase the distance between the phase-gratings. Whereas Eq. 3 is considering the neutron gravitation fall relative to the

moiré period at the camera, a three-PGMI has the capability to consider the neutron gravitation fall relative to the phase-grating period: $\phi_g \propto 2\pi\Delta_y/p_G$. This can provide an amplification to phase sensitivity by several orders of magnitude.

ACKNOWLEDGEMENTS

This work was supported by the Canadian Excellence Research Chairs (CERC) program, the Natural Sciences and Engineering Research Council of Canada (NSERC) Discovery program, Collaborative Research and Training Experience (CREATE) program, the Canada First Research Excellence Fund (CFREF), and the National Institute of Standards and Technology (NIST) and the US Department of Energy, Office of Nuclear Physics, under Interagency Agreement 89243019SSC000025. The pulsed neutron experiment at J-PARC MLF was performed under a user program (Proposal No. 2022A0104).

-
- [1] Roberto Colella, Albert W Overhauser, and Samuel A Werner, “Observation of gravitationally induced quantum interference,” *Physical Review Letters* **34**, 1472 (1975).
 [2] Helmut Rauch, Anton Zeilinger, Gerald Badurek, A Wilfing, W Bauspiess, and U Bonse, “Verification of coherent spinor rotation of fermions,” *Physics Letters A* **54**, 425–427 (1975).
 [3] Yuji Hasegawa, Rudolf Loidl, Gerald Badurek, Katharina Durstberger-Rennhofer, Stephan Sponar, and Helmut Rauch, “Engineering of triply entangled states in a single-neutron system,” *Physical Review A* **81**, 032121 (2010).
 [4] Christopher J Wood, Mohamed O Abutaleb, Michael G Huber, Muhammad Arif, David G Cory, and Dmitry A Pushin, “Quantum correlations in a noisy neutron interferometer,” *Physical Review A* **90**, 032315 (2014).
 [5] Charles W Clark, Roman Barankov, Michael G Huber, Muhammad Arif, David G Cory, and Dmitry A Pushin, “Controlling neutron orbital angular momentum,” *Nature* **525**, 504–506 (2015).
 [6] Dusan Sarenac, Michael G Huber, Benjamin Heacock, Muhammad Arif, Charles W Clark, David G Cory, Chandra B Shahi, and Dmitry A Pushin, “Holography with a neutron interferometer,” *Optics Express* **24**, 22528–22535 (2016).

- [7] Hartmut Lemmel, Ph Brax, AN Ivanov, Tobias Jenke, Guillaume Pignol, Mario Pitschmann, Thomas Potocar, Markus Wellenzohn, Michael Zawisky, and Hartmut Abele, “Neutron interferometry constrains dark energy chameleon fields,” *Physics Letters B* **743**, 310–314 (2015).
- [8] Ke Li, Muhammad Arif, David G Cory, Robert Haun, Benjamin Heacock, Michael G Huber, Joachim Nsofini, Dimitry A Pushin, Parminder Saggu, Dusan Sarenac, *et al.*, “Neutron limit on the strongly-coupled chameleon field,” *Physical Review D* **93**, 062001 (2016).
- [9] AG Klein and SA Werner, “Neutron optics,” *Reports on Progress in Physics* **46**, 259 (1983).
- [10] Hartmut Abele, “The neutron. its properties and basic interactions,” *Progress in Particle and Nuclear Physics* **60**, 1–81 (2008).
- [11] Bertram Terence Martin Willis and Colin J Carlile, *Experimental neutron scattering* (Oxford University Press, 2017).
- [12] WT Fuhrman, J Leiner, P Nikolić, L DeBeer-Schmitt, J-M Mignot, SM Koochpayeh, *et al.*, “Interaction driven subgap spin exciton in the kondo insulator SmB_6 ,” *Physical review letters* **114**, 036401 (2015).
- [13] Fengjiao Qian, Lars J Bannenberg, Heribert Wilhelm, Grégory Chaboussant, Lisa M Debeer-Schmitt, Marcus P Schmidt, Aisha Aqeel, Thomas TM Palstra, Ekkes Brück, Anton JE Lefering, *et al.*, “New magnetic phase of the chiral skyrmion material Cu_2OSeO_3 ,” *Science Advances* **4**, eaat7323 (2018).
- [14] CD Dewhurst, M Mochizuki, K Yanai, *et al.*, “Néel-type skyrmion lattice with confined orientation in the polar magnetic semiconductor GaV_4S_8 ,” *Nature materials* **14**, 1116–1122 (2015).
- [15] ME Henderson, B Heacock, M Bleuel, DG Cory, C Heikes, MG Huber, J Krzywon, O Nahman-Levesqué, GM Luke, M Pula, *et al.*, “Three-dimensional neutron far-field tomography of a bulk skyrmion lattice,” *Nature Physics* , 1–7 (2023).
- [16] Helmut Rauch and Samuel A Werner, *Neutron interferometry: lessons in experimental quantum mechanics* (Oxford University Press, New York, 2015).
- [17] Parminder Saggu, Taisiya Mineeva, Muhammad Arif, DG Cory, Robert Haun, Ben Heacock, MG Huber, Ke Li, Joachim Nsofini, Dusan Sarenac, *et al.*, “Decoupling of a neutron interferometer from temperature gradients,” *Review of Scientific Instruments* **87**, 123507 (2016).
- [18] John F. Clauser and Shifang Li, “Talbot-vonLau atom interferometry with cold slow potassium,” *Physical Review A* **49**, R2213–R2216 (1994).
- [19] F Pfeiffer, C Grünzweig, O Bunk, G Frei, E Lehmann, and C David, “Neutron Phase Imaging and Tomography,” *Physical Review Letters* **96**, 215505 (2006).
- [20] Alexander D Cronin and Ben McMorrnan, “Electron interferometry with nanogratings,” *Physical Review A* **74**, 061602 (2006).
- [21] C David, B Nöhammer, H H Solak, and E Ziegler, “Differential x-ray phase contrast imaging using a shearing interferometer,” *Applied Physics Letters* **81**, 3287–3289 (2002).
- [22] Alexander D. Cronin, Jörg Schmiedmayer, and David E. Pritchard, “Optics and interferometry with atoms and molecules,” *Reviews of Modern Physics* **81**, 1051–1129 (2009).
- [23] Michael S Chapman, Christopher R Ekstrom, Troy D Hammond, Jörg Schmiedmayer, Bridget E Tannian, Stefan Wehinger, and David E Pritchard, “Near-field imaging of atom diffraction gratings: The atomic talbot effect,” *Physical Review A* **51**, R14 (1995).
- [24] Matteo Busi, Jiazhou Shen, Michael Bacak, Marie Christine Zdora, Jan Čapek, Jacopo Valsecchi, and Markus Strobl, “Multi-directional neutron dark-field imaging with single absorption grating,” *Scientific Reports* **13**, 15274 (2023).
- [25] H.F. Talbot, “Lxxxvi. facts relating to optical science. no. iv,” *Philosophical Magazine Series 3* **9**, 401–407 (1836).
- [26] Houxun Miao, Alireza Panna, Andrew A Gomella, Eric E Bennett, Sami Znati, Lei Chen, and Han Wen, “A universal moire effect and application in x-ray phase-contrast imaging,” *Nature Physics* (2016).
- [27] Dmitry A Pushin, Dusan Sarenac, Daniel S Hussey, Haixing Miao, Muhammad Arif, David G Cory, Michael G Huber, David L Jacobson, Jacob M LaManna, Joseph D Parker, *et al.*, “Far-field interference of a neutron white beam and the applications to noninvasive phase-contrast imaging,” *Physical Review A* **95**, 043637 (2017).
- [28] Daniel S Hussey, Houxun Miao, Guangcui Yuan, Dmitry Pushin, Dusan Sarenac, Michael G Huber, David L Jacobson, Jacob M LaManna, and Han Wen, “Demonstration of a white beam far-field neutron interferometer for spatially resolved small angle neutron scattering,” *arXiv preprint arXiv:1606.03054* (2016).
- [29] Dusan Sarenac, Dimitry A Pushin, Michael G Huber, Daniel S Hussey, Haixing Miao, Muhammad Arif, David G Cory, Alexander D Cronin, Benjamin Heacock, David L Jacobson, *et al.*, “Three phase-grating moiré neutron interferometer for large interferometer area applications,” *Physical Review Letters* **120**, 113201 (2018).
- [30] Adam J Brooks, Daniel S Hussey, Hong Yao, Ali Haghshenas, Jumao Yuan, Jacob M LaManna, David L Jacobson, Caroline G Lowery, Nikolay Kardjilov, Shengmin Guo, *et al.*, “Neutron interferometry detection of early crack formation caused by bending fatigue in additively manufactured ss316 dogbones,” *Materials & Design* **140**, 420–430 (2018).
- [31] Adam J Brooks, Gerald L Knapp, Jumao Yuan, Caroline G Lowery, Max Pan, Bridget E Cadigan, Shengmin Guo, Daniel S Hussey, and Leslie G Butler, “Neutron imaging of laser melted ss316 test objects with spatially resolved small angle neutron scattering,” *Journal of Imaging* **3**, 58 (2017).
- [32] Dusan Sarenac, Melissa E Henderson, Huseyin Ekinci, Charles W Clark, David G Cory, Lisa DeBeer-Schmitt, Michael G Huber, Connor Kapahi, and Dmitry A Pushin, “Experimental realization of neutron helical waves,” *Science Advances* **8**, eadd2002 (2022).
- [33] John Frederick Nye and Michael Victor Berry, “Dislocations in wave trains,” *Proceedings of the Royal Society of London. A. Mathematical and Physical Sciences* **336**, 165–190 (1974).
- [34] Ronald O Nelson, Sven C Vogel, James F Hunter, Erik B Watkins, Adrian S Losko, Anton S Tremsin, Nicholas P Borges, Theresa E Cutler, Lee T Dickman, Michelle A Espy, *et al.*, “Neutron imaging at lances—from cold to ultrafast,” *Journal of Imaging* **4**, 45 (2018).
- [35] Takenao Shinohara, Tetsuya Kai, Kenichi Oikawa, Takeshi Nakatani, Mariko Segawa, Kosuke Hiroi, Yuhua Su, Motoki Ooi, Masahide Harada, Hiroshi Iikura, *et al.*,

- “The energy-resolved neutron imaging system, raden,” Review of Scientific Instruments **91** (2020).
- [36] D Sarenac, G Gorbet, C Kapahi, Charles W Clark, DG Cory, H Ekinci, S Fangzhou, ME Henderson, MG Huber, D Hussey, *et al.*, “Cone beam neutron interferometry: from modeling to applications,” arXiv preprint arXiv:2309.01787 (2023).
- [37] Peter Milde, Denny Köhler, Joachim Seidel, LM Eng, Andreas Bauer, Alfonso Chacon, Jonas Kindervater, Sebastian Mühlbauer, Christian Pfeiderer, Stefan Buhandt, *et al.*, “Unwinding of a skyrmion lattice by magnetic monopoles,” Science **340**, 1076–1080 (2013).
- [38] X. Yu, J. Masell, F. S. Yasin, K. Karube, N. Kanazawa, K. Nakajima, T. Nagai, K. Kimoto, W. Koshibae, Y. Taguchi, N. Nagaosa, and Y. Tokura, “Real-space observation of topological defects in extended skyrmion-strings,” Nano Letters **20**, 7313–7320 (2020).
- [39] Certain trade names and company products are mentioned in the text or identified in an illustration in order to adequately specify the experimental procedure and equipment used. In no case does such identification imply recommendation or endorsement by the National Institute of Standards and Technology, nor does it imply that the products are necessarily the best available for the purpose.

APPENDIX

A. Phase-grating fabrication

Double-side polished 10.16 cm diameter (100) silicon wafers were used to fabricate these gratings. A bilayer resist (PMGI/S1805 [39]) was patterned via a maskless aligner (MLA 150, Heidelberg Instrument). As a hard mask for the plasma etching, Cr metal (60 nm) was e-beam evaporated and lifted-off in heated PG Remover. A Bosch recipe was adopted to achieve a vertical sidewall etch profile. The samples were etched in an Oxford PlasmaLab ICP-380 inductively coupled plasma reactive ion etching (ICP-RIE) system, which provides high-density plasma with independently controlled system parameters. In our Bosch recipe, the passivation half cycle comprises the RF chuck power: 5 W, ICP coil power: 1000 W, C4F8: 160 sccm, pressure: 2.67 Pa, temperature: 15 °C for 5 s while the etch half cycle comprises the RF chuck power: 100 W, ICP coil power: 1000 W, SF6: 160 sccm, pressure: 3.33 Pa, temperature: 15 °C for 4 s. After fabricating the gratings, the remaining Cr mask was removed via plasma etching. Fig. 5 shows the SEM images of the four types of phase-gratings that were fabricated.

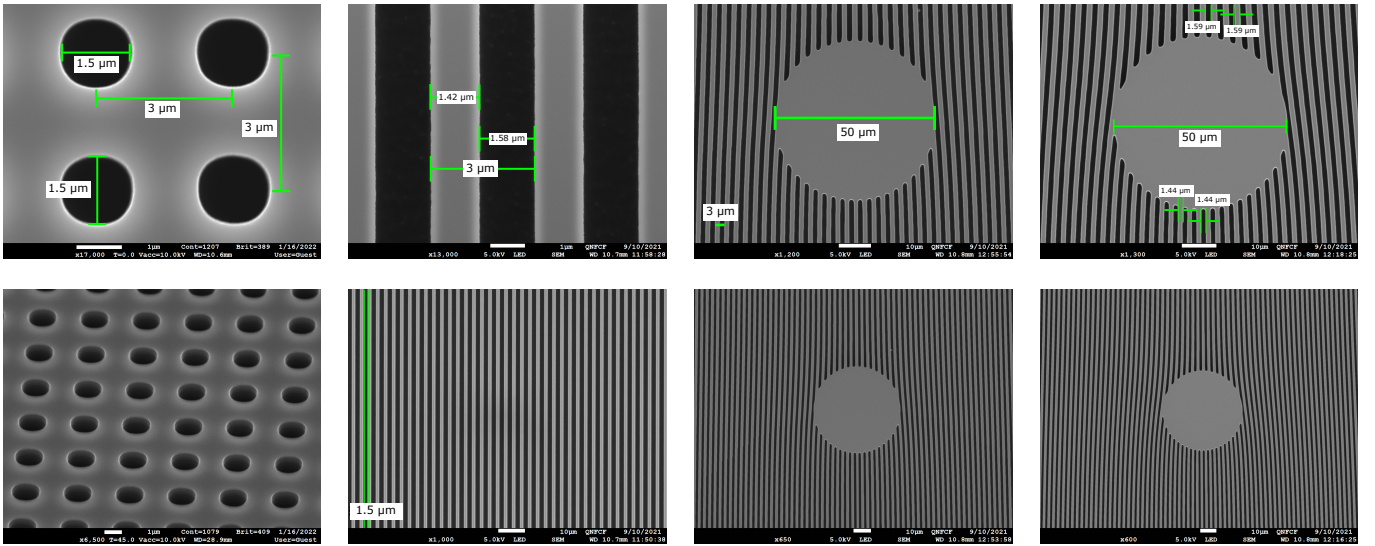


FIG. 5. SEM profiles of the phase-gratings used in the experiments. All phase-gratings were fabricated out of silicon and had a target period of $3 \mu\text{m}$ and height $8.53 \mu\text{m}$. The first column depicts the 2D phase-gratings, the second, third, fourth column shows the fork-dislocation phase-grating with $q = 0, 4, 7$, respectively. The $q = 0$ are the typical 1D phases-gratings. There was a $50 \mu\text{m}$ mask covering the middle region of the $q = 4$ and $q = 7$ fork-dislocation phase-gratings. This is a common practice to avoid the fabrication challenges associated with the higher aspect ratio near the phase-singularity. In regards to the presented PGMI configurations, the masked region sets the limit on the resolution of the observable moiré phase-singularity to $\approx 100 \mu\text{m}$. Therefore the effect of this masked region is negligible.

B. Wavelength Distributions

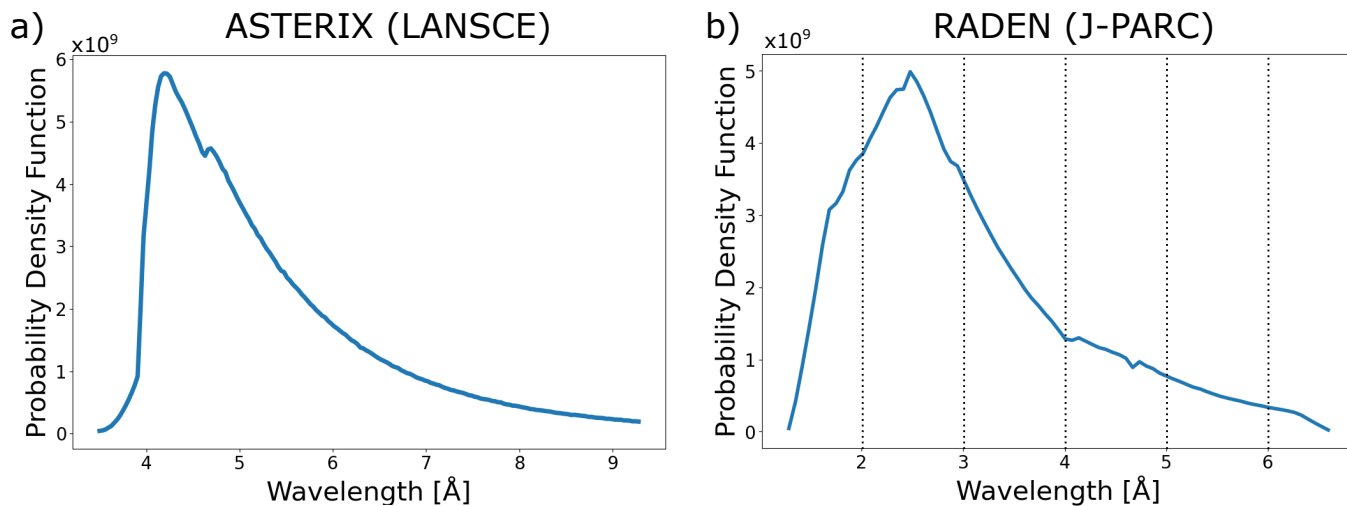


FIG. 6. a) The wavelength distribution for the ASTERIX facility at the Los Alamos Neutron Science Center (LANSCE). This wavelength distribution was used for the data presented in Fig. 1d and Fig. 2. b) The wavelength distribution for the RADEN facility at the Japan Proton Accelerator Research Complex (J-PARC). This wavelength distribution was used for the data presented in Fig. 3c and Fig. 4. The vertical lines show the 4 regions of the time-of-flight data used in Figs. 4b & 4c.